ORIGINAL RESEARCH ARTICLE

Factors Distinguishing Hydrogen-Assisted Intergranular and Intergranular-Like Fractures in a Tempered Lath Martensitic Steel

TINGSHU CHEN, TAKAHIRO CHIBA, MOTOMICHI KOYAMA, EIJI AKIYAMA, and KENICHI TAKAI

Intergranular fracture is the primary fracture mode when a significant amount of hydrogen is introduced into lath martensitic steels. When the introduced hydrogen content is reduced, the contribution of plasticity in the intergranular fracture is significant. Specifically, the crack path is still along prior austenite grain boundaries, but there are some signs of activation of the ductile mechanism (*i.e.,* the tear ridges) on the fracture surface. The plasticity-assisted fracture mode is classified as an intergranular-like fracture. To characterize the difference between intergranular and intergranular-like fractures, these two hydrogen-assisted fracture modes were analyzed in terms of crack path, crack morphology, and local plasticity evolutions. Intergranular fracture occurred in the macroscopically elastic regime with a significant portion of smooth regions on the fracture surface. The intergranular crack growth was discontinuous at the grain size scale, and the preferential microstructure preventing the crack growth was triple junctions of the prior austenite grain boundary. For intergranular-like fracture, plasticity significantly evolved during crack growth, which caused nano-voids in the vicinity of the crack tip. Coalescence of the crack and nano-voids resulted in intergranular-like crack growth along prior austenite grain boundaries. The coalescence with nano-voids caused tear ridges on the intergranular-like fracture surface.

https://doi.org/10.1007/s11661-022-06608-2
© The Minerals, Metals & Materials Society and ASM International 2022

I. INTRODUCTION

LATH martensitic steel is widely used for making lightweight automobile components because of its combination of high tensile strength (over 1 GPa) and excellent ductility. The high tensile strength is related not only to the high toughness of the unit microstructure (*i.e.,* lath), but also the hierarchical microstructure of lath martensite[1–3] (including prior austenite grains, packets, blocks, and laths), which refines the matrix structure and increases the area of internal boundaries.[4,5] However, with a balanced strength-ductility combination, lath martensitic steel still faces an inevitable challenge that can severely degrade its in-use mechanical properties, *i.e.,* hydrogen embrittlement.

The presence of internal (from the fabrication process) and/or external (from the service environment) hydrogen can degrade the ductility and ultimate tensile strength (UTS) of steels, resulting in catastrophic and premature failure.[6,7] The fracture mode in lath martensitic steels also changes from conventional micro-void coalescence to two typical hydrogen-induced fracture modes: intergranular (IG)[8–10] and quasi-cleavage (QC)[10–13] fractures. Because of the apparent fracture path along the prior austenite grain boundaries,[9,14–16] IG fracture has been characterized from a fractographic viewpoint in lath martensitic steels. On the other hand, the hydrogen-related micro-mechanisms of QC fracture have been investigated by analyzing the dislocation microstructure evolution, which could enable interpretations of the complex crack morphologies and typical fine features on QC fracture facets (such as tear ridges and river markings).[7,17–19] Furthermore, in the recent work of Ogawa *et al.,*[20] an intermediate fracture mode between IG and QC was observed under certain testing conditions, in which the fracture surface shows a large

TINGSHU CHEN is with the Institute for Materials Research, Tohoku University, 2-1-1 Katahira, Aoba-ku, Sendai, 980-8577, Japan and also with the Graduate School of Engineering, Tohoku University, 6-6 Aramaki Aza Aoba, Aoba-ku, Sendai, Miyagi, 980-8579, Japan. TAKAHIRO CHIBA is with the Graduate School of Science and Technology, Sophia University, Tokyo 102-8554, Japan. MOTOMICHI KOYAMA is with the Institute for Materials Research, Tohoku University and also with the Elements Strategy Initiative for Structural Materials (ESISM), Kyoto University, Yoshida-honmachi, Sakyo-ku, Kyoto 606-8501, Japan. Contact e-mail: koyama@imr.tohoku.ac.jp EIJI AKIYAMA is with the Institute for Materials Research, Tohoku University. KENICHI TAKAI is with the Department of Engineering and Applied Science, Sophia University, Tokyo 102-8554, Japan.
Manuscript submitted October 14, 2021; accepted January 17, 2022.
Article published online March 15, 2022

number of tear ridges on the IG fracture surface; this characteristic fracture mode is classified as intergranular-like (IG-like) fracture. In our recent research, the fine fractographic features (e.g., tear ridges and river markings) on QC fracture facets were clarified to be the result of local strain evolution and the interaction between cracks and hierarchical boundaries in lath martensite.[21] In this context, the occurrence of IG-like fracture indicates that the plasticity and hierarchical microstructure also play a key role in both crack initiation and crack growth, even on/near the prior austenite grain boundaries in the hydrogen-charged lath martensitic steel.

With respect to IG fracture in lath martensitic steels, although a consensus has not necessarily been reached, the direct effect of hydrogen, which reduces the cohesive energy of prior austenite grain boundaries, has been proposed as the primary mechanism for IG crack formation (*i.e.,* hydrogen-enhanced decohesion (HEDE)).[14,22,23] In contrast, although IG-like cracks also grow and propagate along the prior austenite grain boundaries, the mechanisms underlying the superimposed fracture morphology (*i.e.,* the tear ridges on IG facets) are unclear. In previous studies, Nagumo and Matsuda suggested that hydrogen increases the density of strain-induced vacancies, leading to IG fracture with tear ridges.[24] Nagao et al. highlighted the role of another primary hydrogen-related mechanism, *i.e.,* hydrogen-enhanced localized plasticity (HELP),[25–28] in crack initiation and crack growth on prior austenite grain boundaries.[29] Shibata et al. also proposed that the high accumulation of hydrogen around the prior austenite grain boundaries enhances local dislocation motion, resulting in the formation of microcracks near prior austenite grain boundaries.[30] Although IG-like fracture has been characterized in terms of fractographic features, the specific roles of plasticity in both IG and IG-like cracking behaviors, especially in the crack initiation and growth stages, are not yet understood. In addition, the interaction between the crack and hierarchical microstructure in lath martensite affects the local strain evolution, which further complicates the hydrogen-assisted cracking behavior. Therefore, we comparatively investigated IG and IG-like fracture modes that have the same crack path (*i.e.,* the prior austenite grain boundaries) to clarify the roles of plasticity and hierarchical characteristics in the hydrogen-assisted cracking behavior of IG-like fracture in lath martensite.

Tempered lath martensitic steel was tensile-tested in the present study, exhibiting IG fracture and IG-like fracture, respectively, by varying the hydrogen charging conditions. Morphological features on the fracture surfaces were extracted using scanning electron microscopy (SEM). The microstructural information and local plastic strain distribution around the specific IG/IG-like cracks were analyzed in bulk specimens using SEM-based techniques, including electron channeling contrast imaging (ECCI) and electron backscatter diffraction (EBSD) analysis, to differentiate the two fracture modes. The coupling among the hierarchical martensite structure, crack morphology, local strain evolution, and typical fractographic features (*i.e.,* tear ridges) is discussed to understand the nature of hydrogen-induced IG-like fracture.

II. EXPERIMENTAL PROCEDURE

A. *Material*

We received tempered lath martensitic steel with the chemical composition listed in Table I. Some details, including heat treatment, have been presented elsewhere.[10] The as-received sample shape was cylindrical, and the sample was machined using a lathe to make a gauge section of the tensile specimen. Figure 1 shows the initial microstructures obtained before the tensile tests. The microstructure fully consists of martensite, and fine cementite exists both on the grain boundaries and within the grain interior.[20]

B. *Mechanical Tests and Hydrogen Charging*

Dog-bone-type specimens with gauge dimensions of 5 mm in diameter and 30 mm in length[31] were tensile-tested at a cross-head displacement rate of 0.01 mm/min at ambient temperature. Prior to the tests, the tensile specimens were mechanically polished using emery papers #1000 and #2000. To obtain specimens that showed IG and IG-like fracture surfaces, hydrogen charging was conducted before and during tensile tests at a current density of 100 A/m^2 in an aqueous solution of 0.1 N NaOH with and without 5 g/L NH_4SCN. Hydrogen charging prior to the tensile tests was performed at 30 °C for 96 hours. Three specimens used for measuring the hydrogen content were mechanically polished, and two of them were electrochemically charged with hydrogen in the same solution at the same current density as those used for the tensile tests; the third one was used as a blank. The hydrogen content was measured by thermal desorption analysis (TDA) using a gas chromatograph with a semiconductor gas sensor as the detector at a heating rate of 100 °C/h. The cumulative hydrogen desorbed from ambient temperature to 300 °C was defined as the diffusible hydrogen in the present study, which includes hydrogen weakly trapped at lattice defects such as dislocations and grain boundaries. The diffusible hydrogen has been reported to play a primary role in hydrogen embrittlement.[32,33]

C. *Microstructural Characterization*

The fracture surfaces obtained by tensile testing were observed using secondary electron imaging (SEI) at an accelerating voltage of 15 kV. Two other specimens were prepared by tensile testing, in which the testing process was interrupted immediately after reaching the ultimate tensile strength (UTS), to characterize the microstructures surrounding the IG and IG-like cracks,

Table I. Chemical Composition of the Steel Used (wt Pct)

C	Si	Mn	P	S	Fe
0.30	0.21	0.72	0.019	0.002	Bal.

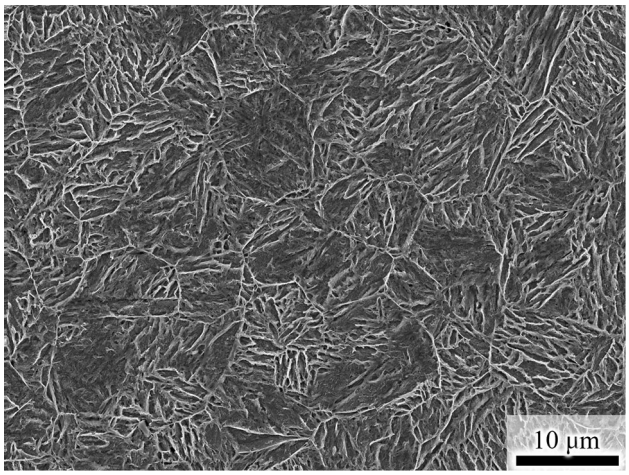

Fig. 1—Initial microstructure before tensile tests. This image was obtained after chemical etching with 5 pct nital.

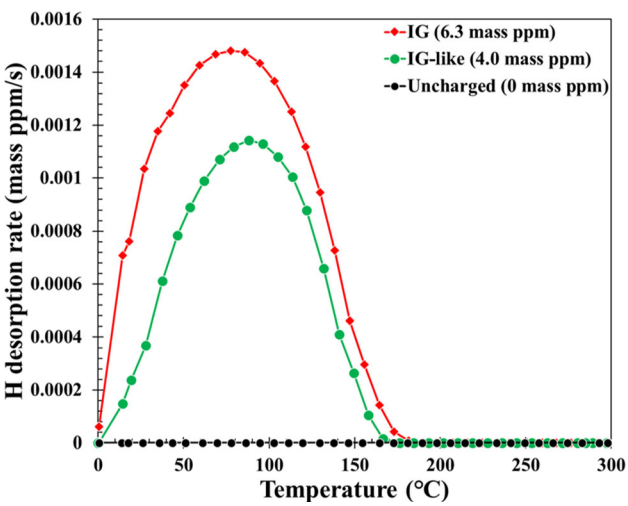

Fig. 2—Hydrogen desorption rate versus temperature curves.

respectively. The microstructures were observed by SEI, ECCI, and EBSD measurements. The specimens for the damage-related microstructural observations were first mechanically ground to obtain a rectangular specimen shape, as ECCI and EBSD require a flat specimen surface. Then, they were mechanically polished to a mirror finish using colloidal silica with a particle size of 60 nm. The ECCI was operated at 30 kV, and EBSD measurements were conducted at 20 kV with a beam step size of 50 nm.

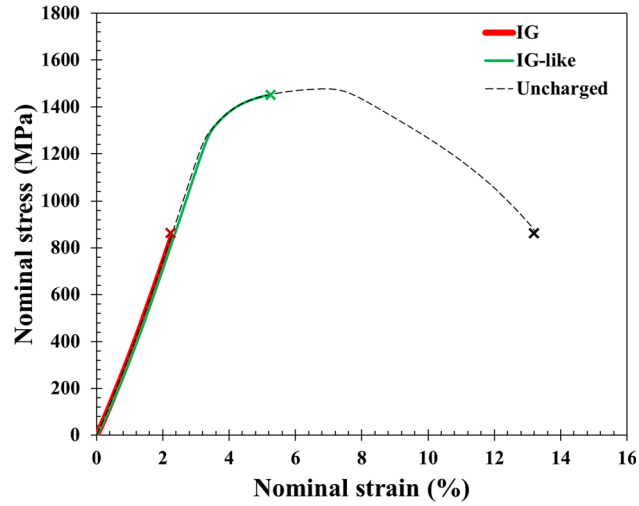

Fig. 3—Nominal stress-strain curves for specimens containing IG fracture and IG-like fracture, as well as the uncharged specimen.

III. RESULTS

A. *Mechanical Tests and Fractographic Features*

Figure 2 shows the TDA profiles of the hydrogen-uncharged and hydrogen-charged specimens. Hydrogen charging with and without NH_4SCN led to a single peak and diffusible hydrogen contents of 6.3 and 4.0 mass ppm, respectively. No significant hydrogen desorption was detected in the uncharged specimen; thus, the diffusible hydrogen content was 0 mass ppm.

Figure 3 shows the nominal stress-strain curves obtained in the tensile tests under different hydrogen charging conditions. The uncharged specimen showed necking and subsequent cup-and-cone ductile fracture, as shown in Figure 4(a). The ductile fracture surface was fully covered with dimples, and inclusions were observed on the bottom of the dimples [Figure 4(b)], which indicates that the ductile fracture originated from the inclusion/matrix interface cracking. When the specimen was hydrogen-charged in the solution containing NH_4SCN, the fracture occurred in the elastic regime. The fracture surface is shown in Figure 5(a). Here note that a significant portion of the IG fracture surface did not contain traces arising from plastic activities, as shown in Figure 5(b). When the specimen was hydrogen-charged in the solution without NH_4SCN, premature fracture occurred after yielding, and numerous tear-ridges were present on all the intergranular features of the fracture surface [Figures 5(c) and (d)]. In addition, there were secondary cracks that were related to crack branching/deflection, as indicated by the yellow arrows in Figures 5(a) and (c). In this study, in accordance with the definitions of the previous study,[20] fracture mode that showed the relatively low fraction of the fracture surface involving the plasticity-related traces is referred to as IG fracture, and the fracture surface of which all involved the traces is referred to as IG-like fracture. The number of secondary cracks on the IG-like fracture surface was significantly higher than that on the IG fracture surface.

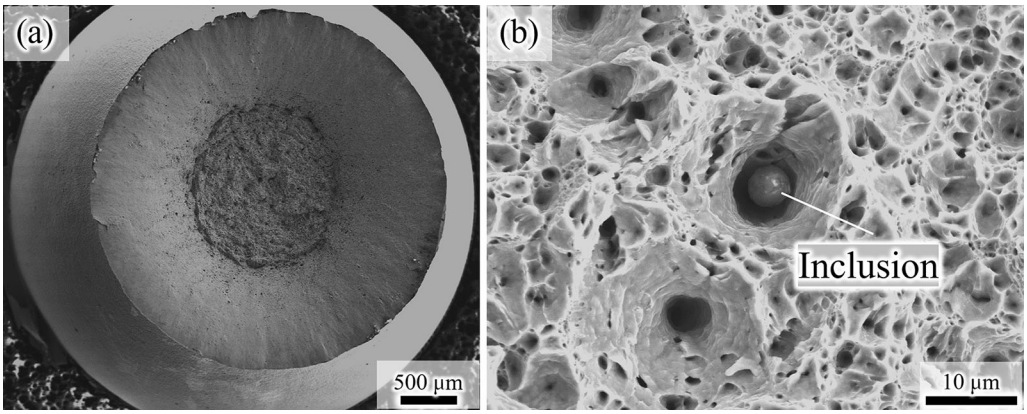

Fig. 4—(*a*) Overview of the fracture surface of hydrogen-uncharged specimen. (*b*) Magnified SE image of dimples on the fracture surface.

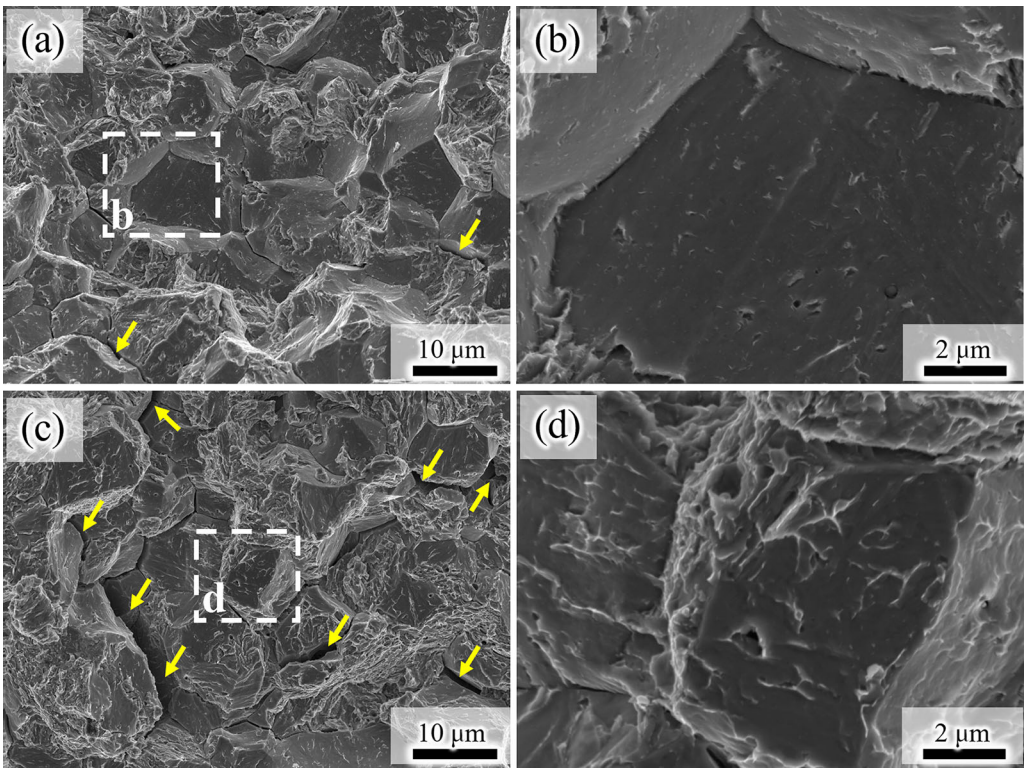

Fig. 5—(*a*) IG fracture surface obtained by tensile testing. (*b*) IG fracture facet at higher magnification. (*c*) IG-like fracture surface obtained by tensile testing. (*d*) IG-like fracture surface at higher magnification. The yellow arrows in (a) and (c) indicate sub-cracks (Color figure online).

B. *Crack Morphologies and Microstructure Evolution*

To clarify the specific roles of the plasticity and hierarchical characteristics in IG and IG-like fractures, the tensile tests for hydrogen-charged specimens were interrupted when reaching the maximum stress which was immediately before the final rupture. This enables to observe the internal hydrogen-assisted IG/IG-like cracks and the associated microstructures surrounding the cracks. Figure 6(a) shows the specimen configuration obtained from the interrupted tensile tests and subsequent mechanical polishing, and the crack morphologies of IG fracture and IG-like fracture are shown in Figures 6(b) and (c), respectively. Clearly, the IG-like crack shows larger degrees of crack opening, crack deflection, and crack branching than the IG crack. In addition, numerous sub-cracks were observed near the large IG-like cracks.

Figure 7 shows the EBSD measurement results for the IG fracture. Figure 7(a) is an image quality (IQ) map that reflects the quality of the Kikuchi line for each measurement,[34] exhibiting both the crack morphology and the hierarchical microstructures surrounding the crack.[3,35] The white dashed, yellow, and black lines in Figure 7(c) indicate the boundaries of the prior austenite grain, packet, and block, respectively [Figure 7(b)], according to the crystallographic analysis.[2,3] The colors in the RD-IPF map [Figure 7(c)] correspond to the

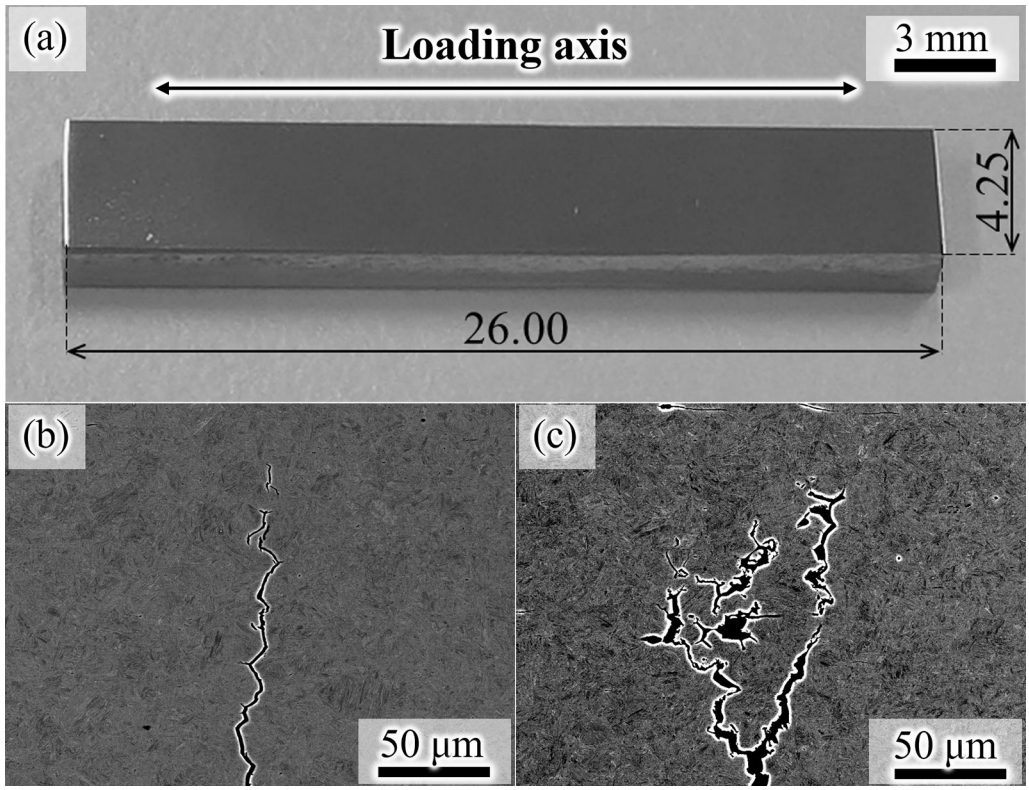

Fig. 6—(*a*) Polished rectangular specimen obtained by interrupted tensile tests for microstructure observation. (*b*) Overview of the crack morphology of IG fracture. (*c*) Overview of the crack morphology of IG-like fracture. The insets in (b) and (c) indicate magnified IG and IG-like cracks.

crystallographic orientation parallel to the loading direction, clearly showing the detailed morphologies of the lath martensite structure. The crack path is marked by red dashed lines, and the crack primarily grows along the prior austenite grain boundaries [Figure 7(c)]. However, there are two regions, marked by white rectangles in Figure 7(a), that show cracking behavior within the prior austenite grains. The magnifications of the two regions are shown in Figures 8 and 9, respectively. The first region [Figure 8(a)] indicates a microscale crack initiated within a prior austenite grain. Specifically, the crack occurred along the block boundary with a misorientation angle of 60 deg, according to the IPF map in Figure 8(b). The low KAM values surrounding the crack shown in Figure 8(c) indicate that either the degree of plastic strain evolution during crack initiation and growth was small or the zone size of the localized plasticity was smaller than the spatial resolution of the EBSD measurement.

Figure 9(a) shows the other case exhibiting a crack crossing the prior austenite grain. No obvious plastic strain concentration was involved in the IG crack growth, as evident from the Kernel average misorientation (KAM) map [Figure 7(d)], which corresponds to the geometrically necessary dislocation density and related plastic strain.[35–37] It is noteworthy that the KAM values near the portion of the crack that grew within the prior austenite grain were comparable to those in the IG crack region [Figure 9(b)]. Based on the crystallographic analysis, the crack path within the prior austenite grain was determined to be along the packet boundaries (highlighted by yellow lines, whose misorientation angles were 54, 44, and 47 deg, respectively) within the prior austenite grain [Figure 8(a)]. As the crack grew along the packet boundaries when crossing the prior austenite grain, the fracture facet of the crack within the grain was much rougher than that along the grain boundaries, as shown in Figure 9(c). Furthermore, both the separated packet boundaries and the separated prior austenite grain boundaries [shown in the inset of Figure 9(c)] were almost perpendicular to the loading axis.

An example of the crack branching of IG fracture is shown in Figure 10. The combination of the ECC image and RD-IPF map clearly demonstrates that IG crack branching occurred along the prior austenite grain boundaries. In addition, crack coalescence was also observed, as indicated by the black dashed arrows. According to the IPF map in Figure 10(b), two separate IG cracks coalesced with each other in the transgranular (TG) cracking path.

C. *Crack Morphologies and Microstructure Evolution of IG-Like Fracture*

Figure 11 shows EBSD measurement results around an IG-like crack. The IQ image exhibits the IG-like crack morphology as well as typical lath martensitic microstructures. The martensite boundaries were identified in the same way as in the IG fracture case[2,3]

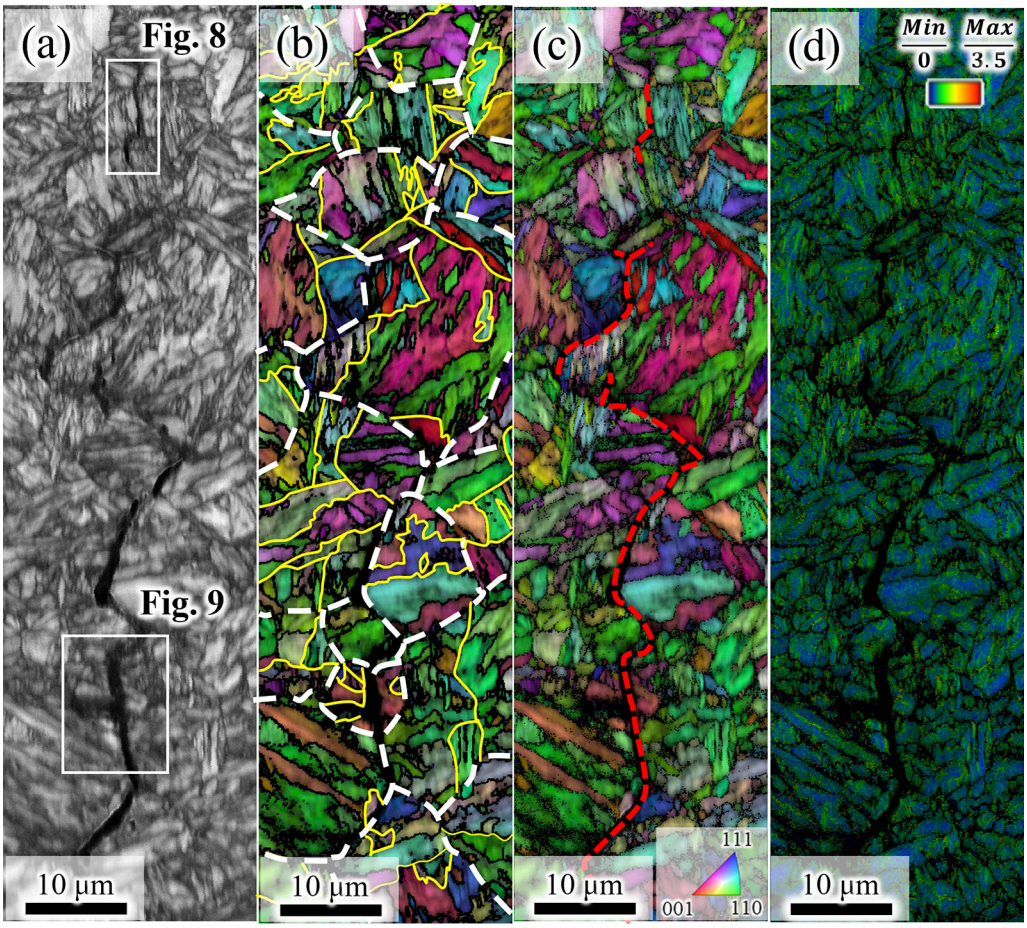

Fig. 7—(*a*) IQ map of IG fracture. (*b*) Identification of hierarchical boundaries in lath martensite. The white dashed, yellow, and black lines represent the boundaries of prior austenite grain, packet, and block, respectively. (*c*) RD-IPF and (*d*) KAM maps of IG fracture. Red dashed lines in (c) represent IG crack path (Color figure online).

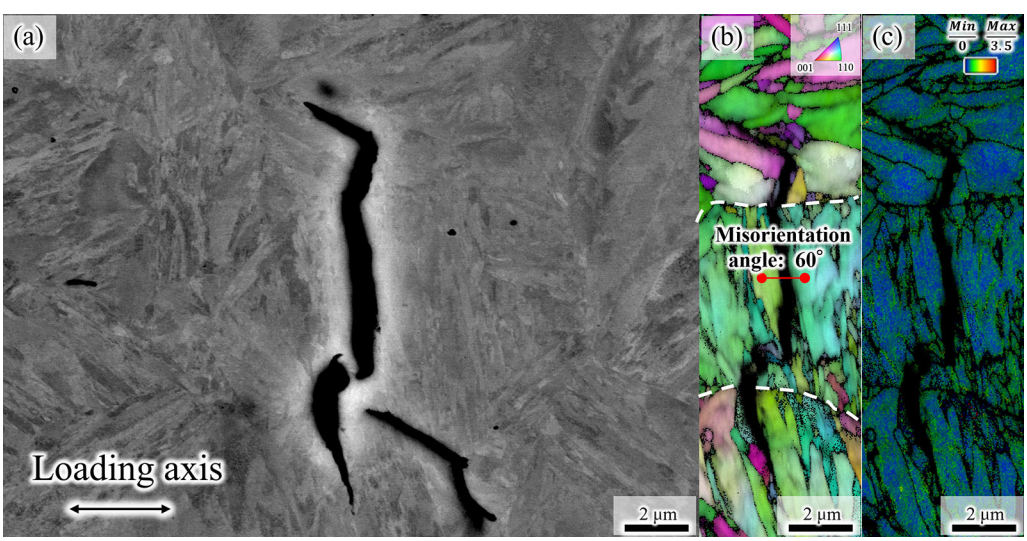

Fig. 8—(*a*) ECC image of crack initiation region marked in Fig. 6(b). (*b*) RD-IPF and (*c*) KAM maps of IG crack initiation. White dashed lines in (b) indicate prior austenite grain boundaries.

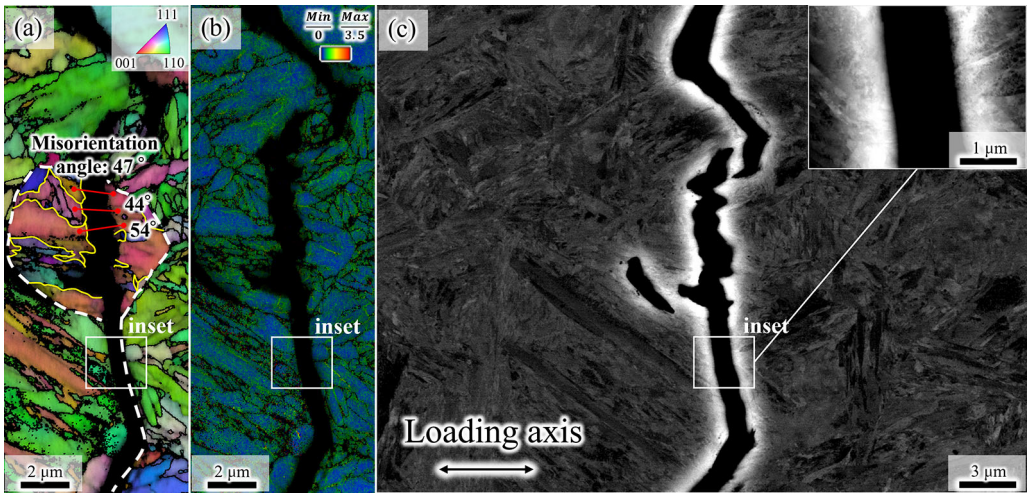

Fig. 9—(*a*) RD-IPF and (*b*) KAM maps of fracture mode transition marked in Fig. 6(b). (*c*) ECC image of fracture mode transition. The white dashed, yellow, and black lines in (*a*) represent the boundaries of prior austenite grain, packet, and block, respectively. The angle values in (a) indicate misorientations between the red points near both sides of the crack (Color figure online).

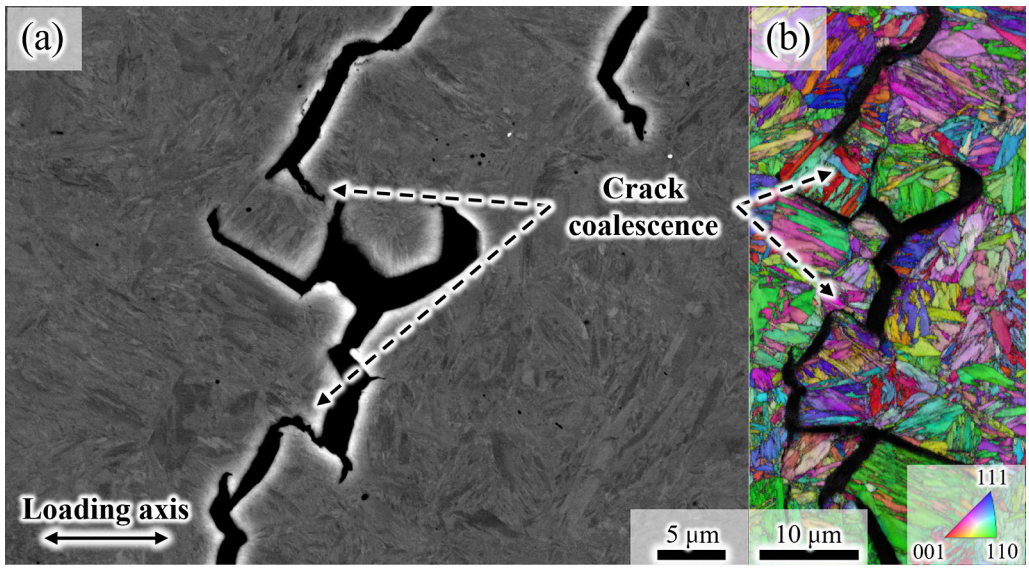

Fig. 10—(*a*) ECC image of IG crack branching. (*b*) RD-IPF map of IG crack branching. The dashed arrows indicate the region where crack coalescence occurred.

[Figure 11(b)]. Red dashed lines in the RD-IPF map [Figure 11(c)] represent the crack path. The combination of Figures 11(b) and (c) indicates that the IG-like crack primarily grew along the prior austenite grain boundaries, similar to IG cracks. As an important difference from IG cracks, the region surrounding the IG-like crack showed higher KAM values than that around the IG crack [Figure 11(d)], which indicates a significant number of dislocations were introduced before and during the IG-like crack growth.

Figure 12 shows the morphology of the IG-like crack tip. According to the crystallographic analysis and the crack path identification in Figures 11(b) and (c), IG-like crack growth [Figure 12(a)] was prevented by a prior austenite grain, and crack branching occurred. Two IG-like crack branches grew along prior austenite grain boundaries. The high-magnification ECC image of the right crack branch [Figure 12(b)] shows a crack tip that is about to coalesce with an enlarged void. Furthermore, there is a row of black dots (marked by yellow arrowheads) that were located at a distance from the crack tip. Because black dots were also observed in the SE image [Figure 12(c)], they were identified as nano-voids. Based on the martensite boundary characterization in the RD-IPF map [Figure 12(d)], the IG-like crack growth (including nano-void formation, growth, and coalescence) occurred along the prior austenite grain boundary (highlighted by the white dashed line). The block alignment directions were different on both sides of the grain boundary; the alignment was almost perpendicular to the grain boundary on the left side and nearly parallel to the grain boundary on the right side

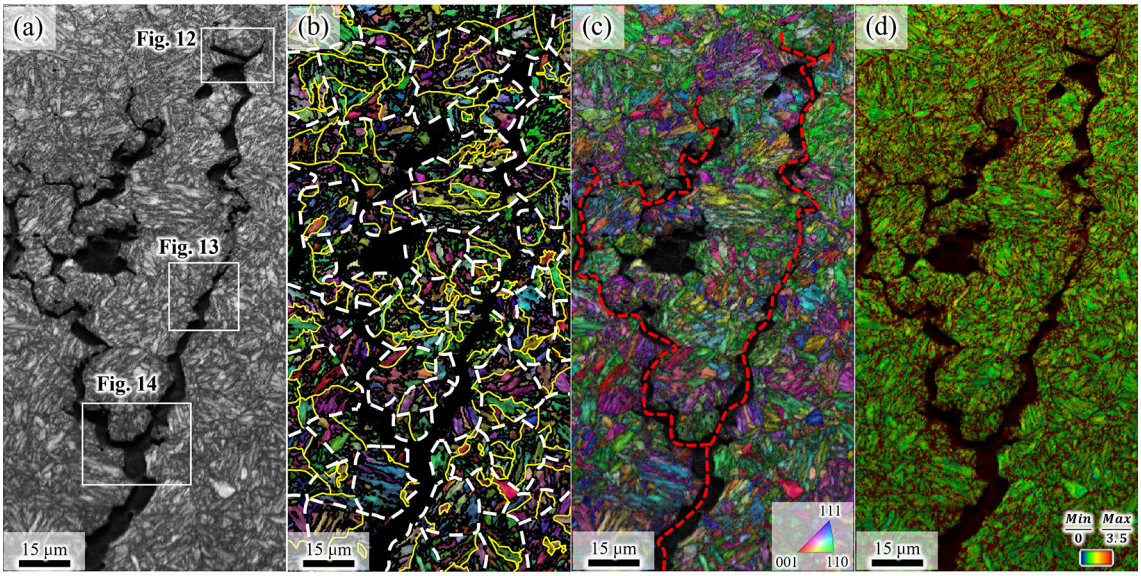

Fig. 11—(*a*) IQ map of IG-like fracture. (*b*) Identification of hierarchical boundaries in lath martensite. The white dashed, yellow, and black lines represent the boundaries of prior austenite grain, packet, and block, respectively. (*c*) RD-IPF and (*d*) KAM maps of IG-like fracture. Red dashed lines in (c) represent the crack path (Color figure online).

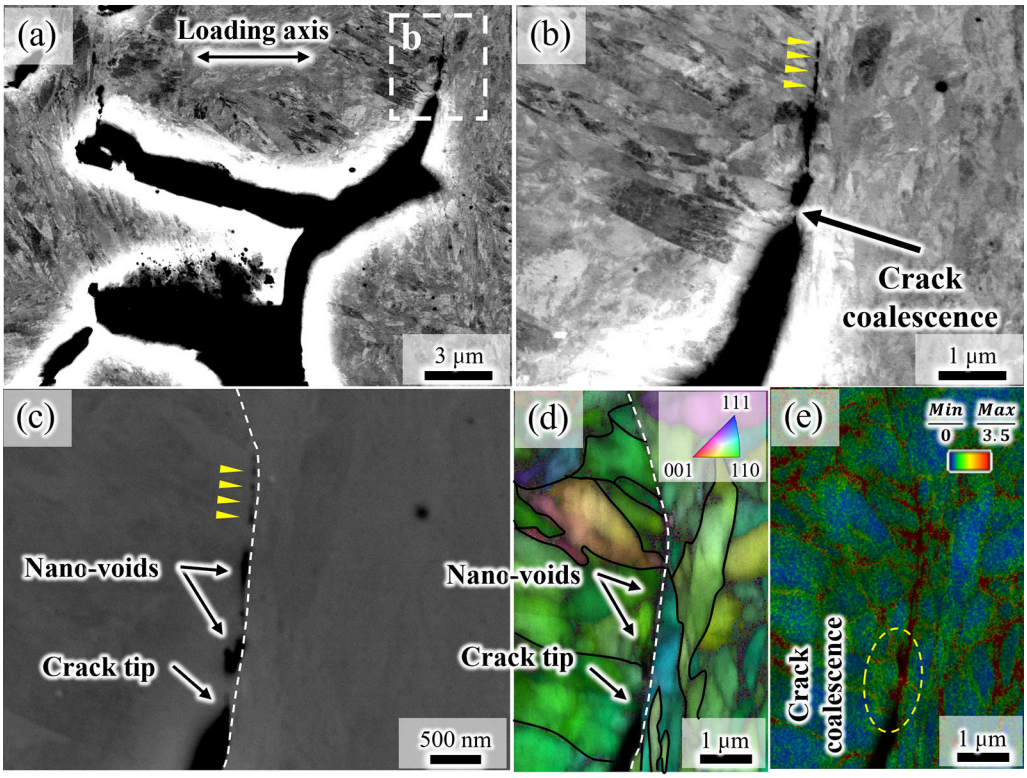

Fig. 12—(*a*) ECC image of the crack tip of IG-like fracture. (*b*) High-magnification ECC image of marked region in (a). SE image of the sharp crack tip and nano-voids. (*d*) RD-IPF and (*e*) KAM maps of hierarchical microstructures surrounding the crack tip. The yellow arrowheads point to tiny voids. The white dashed line in (*c*) and (d) represents the prior austenite grain boundary. The black lines in (d) represent the block boundaries (Color figure online).

(as highlighted by the black lines in Figure 12(d)). Furthermore, both the crack and the nano-voids were formed on the left side of the prior austenite grain boundary, where the blocks were aligned perpendicularly. In Figure 12(e), high KAM values occurred in the vicinity of the IG-like crack tip, especially in the crack coalescence region, which is highlighted by a yellow dashed ellipse. It is also

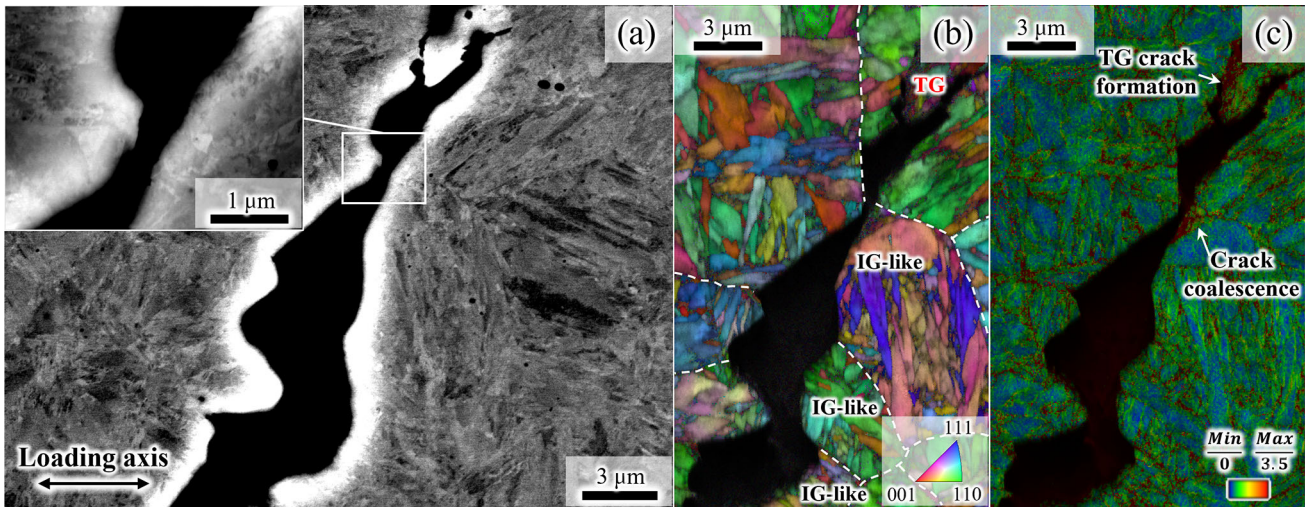

Fig. 13—(*a*) ECC image of the crack morphology of IG-like fracture. (*b*) RD-IPF map and (*c*) KAM map of the crack morphology of IG-like fracture. White dashed lines in (*b*) reflect the prior austenite grain boundaries.

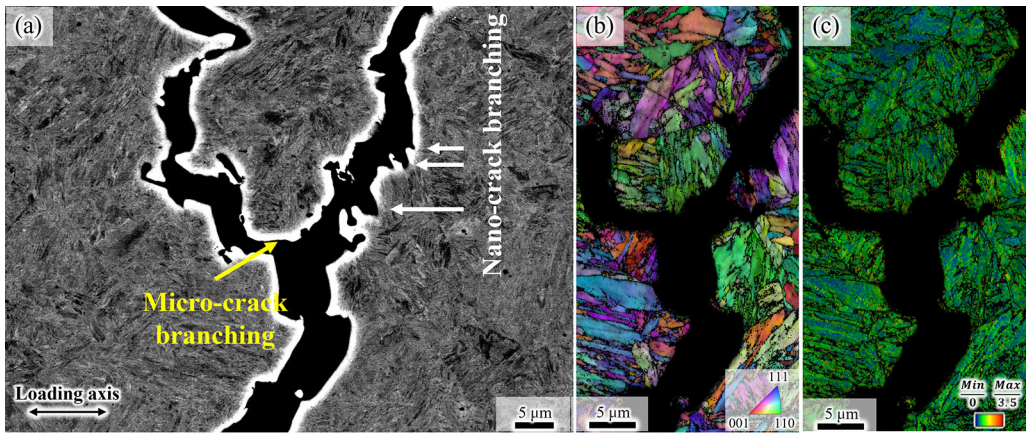

Fig. 14—(*a*) ECC image of crack branching in IG-like fracture. (*b*) RD-IPF and (*c*) KAM maps of the crack branching region in IG-like fracture. Yellow and white dashed rectangles in (a) denote micro-crack branching and nano-crack branching, respectively (Color figure online).

noteworthy that the crack tips which were about to coalesce with each other were located near the prior austenite grain boundary but within the grain.

The ECC image in Figure 13(a) shows the crack morphology of the IG-like fracture, exhibiting a tortuous shape rather than the straight path of the IG fracture [Figure 9(c)]. However, based on the crystallographic orientation analysis and martensite boundary analysis in Figure 13(b), the crack path of the IG-like fracture was still primarily along the prior austenite grain boundaries, even though the fracture mode transition from IG-like to TG was observed. In the KAM map, although the largest local strain evolution occurred within the TG crack growth region, high KAM values were also observed beneath the separated prior austenite grain boundaries, and the spacings between these segregated grain boundaries were different. The inset in Figure 13(a) is a high-magnification ECC image of the location in which crack coalescence occurred between the IG-like and TG cracks, accompanying the obvious local strain evolution shown in the KAM map.

Figure 14(a) shows the crack branching behavior of an IG-like fracture. When the growth of the IG-like crack was arrested by the prior austenite grain [Figure 14(b)], crack branching occurred [marked by a yellow arrow in Figure 14(a)], and the branches grew along the prior austenite grain boundaries. This phenomenon was also observed in the IG fracture condition (Figure 10) and is hereafter referred to as micro-crack branching. However, there was another crack branching behavior, which was highlighted by white arrows. The nano-branches of the crack occurred accompanying the IG-like crack growth and were parallel to the block/lath alignment, according to the RD-IPF map in Figure 14(b). This nano-crack branching phenomenon is seldom observed in IG fractures, whereas it is a typical crack morphology accompanying hydrogen-assisted QC fracture in lath martensitic steels.[21]

IV. DISCUSSION

A. *Microstructure Effects on the Discontinuity of IG Crack Growth*

First, it should be noted that both the IG and IG-like fractures showed intergranular features on the fracture surfaces containing tear ridges, as seen in the overview images (Figures 5(a) and (c)). The important difference in the fracture surface was that the IG fracture showed smooth regions on a significant portion of the fracture surface, which corresponds to the fact that the IG crack path [as shown in the inset of Figure 9(c)] was smooth compared with the IG-like cracks. Furthermore, IG fractures occurred within the linear elastic region (Figure 3). These results imply that the contribution of HEDE in IG crack growth is larger than that in IG-like crack growth. In this context, there were two exceptions showing cracking within prior austenite grains: crack initiation and propagation along the block and packet boundaries. In the following, we first discuss the prior austenite grain boundary cracking, which is the major crack growth path, and then consider the exceptional crack growth behavior, which also provides an important insight into the hydrogen-assisted crack growth mechanism.

Although the boundaries of both prior austenite grains, packets, and blocks are high-angle boundaries,[2,3] the prior austenite grain boundaries are the preferential sites for impurity segregation[38,39] and hydrogen accumulation.[40–42] Thus, hydrogen-related cracks are prone to occur along the prior austenite grain boundaries. Because the KAM values around the crack path were low, less than 1 in some regions [Figure 7(d)], we assume the occurrence of decohesion as a significant mechanism. According to the observation of the region surrounding the IG crack (Figure 7), sub-cracks were initiated at a distance of approximately 10 μm from the tip of the relatively long IG crack. Because the stress concentration between the cracks is significant even when the sub-crack is tens of μm away and inclined to the other crack alignment,[43] the cracks easily show crack coalescence.[44] Therefore, the sub-crack initiation near the crack tip indicates that IG crack growth involves a discontinuous process, *i.e.,* crack coalescence. Because resistance to IG crack growth is dependent on the grain boundary character and local stress acting on the boundary under the assumption that decohesion is the primary factor, the crack can stop once at grain boundary triple junctions. Instead, a new crack would form in the region where the crack tip stress concentration acted. As an extreme case, when the misorientation of a prior austenite grain boundary is low and the grain boundary is not perpendicular to the loading direction, the grain boundary could be a non-preferential crack path, even when IG fracture occurred as the predominant fracture mode. In this case, other high-angle boundaries, such as block and packet boundaries, can also be the cracking path, as shown in Figures 8 and 9. For instance, the block boundary that was cracked in Figure 8 showed a misorientation of 60 deg and was perpendicular to the loading direction. Hence, the observation of cracking along the block and packet boundaries implies that the effects of misorientation and boundary alignment on the cohesive energy and local stress have a significant effect on the hydrogen-assisted IG crack. In other words, the resistance to cracking at prior austenite grain boundaries has a larger deviation that depends on the distribution of misorientation and boundary alignment, which results in a discontinuous crack growth mode at the micron scale. Another important process for discontinuous crack growth is coalescence between the main and sub cracks. Note that TG crack growth occurred in the crack coalescence region, as shown in Figure 10. According to a previous study,[45] cracks can coalesce through dislocation slip when the cracks are close to each other and when an active slip system exists under the stress concentration acting between the cracks. Thus, the occurrence of cracking behavior within the prior austenite grain indicates that the crack coalescence resulted from two cases: (1) IG crack growth and (2) plastic shear in the ligament between the main and sub cracks. Because the KAM values around the IG crack were small everywhere [Figure 7(d)], either the dislocations required for the plastic shear would be emitted to the crack surface or the shear region was smaller than the spatial resolution of the EBSD measurement.

Consequently, IG crack growth, schematically shown in Figure 15, occurred. When the misorientation and alignment of prior austenite grain boundaries were preferable for cracking, IG cracking occurred [Figures 15(a) and (b)]. Once the grain boundary characters could not satisfy the requirements for further growth of the IG crack, the crack growth stopped at the grain boundary triple junction with crack tip blunting [Figures 15(c) and (d)]. Simultaneously, the grain boundary near the blunt crack tip, which was favored for cracking, became the sub-crack initiation site [Figures. 15(d) and (e)]. Then, the newly formed crack coalesced with the blunt crack though IG cracking or plastic shear, enabling further growth of the IG crack. Because the grain boundary characters are the key to IG crack growth, the unit of the crack path became the size of a single prior austenite grain. Because repetition of this process resulted in the final failure, the IG crack growth significantly involved a discontinuous mechanism at the micron scale.

B. *Role of plasticity in the IG-like crack growth*

As seen in the macroscopic view of the IG-like crack [Figures 6(b) and (c)], obvious crack opening, deflection, and branching were observed, of which the degrees were significantly higher than those of the IG crack. These facts indicate that the discontinuous process of the IG-like crack growth was more remarkable than that of the IG crack growth, which could be due to the obvious macroscopic plastic deformation before the final failure (Figure 3). Correspondingly, almost all regions near the crack initiation site contained tear ridges [Figure 5(c)]. Furthermore, the KAM map around the IG-like cracks [Figure 11(d)] showed higher values than those around

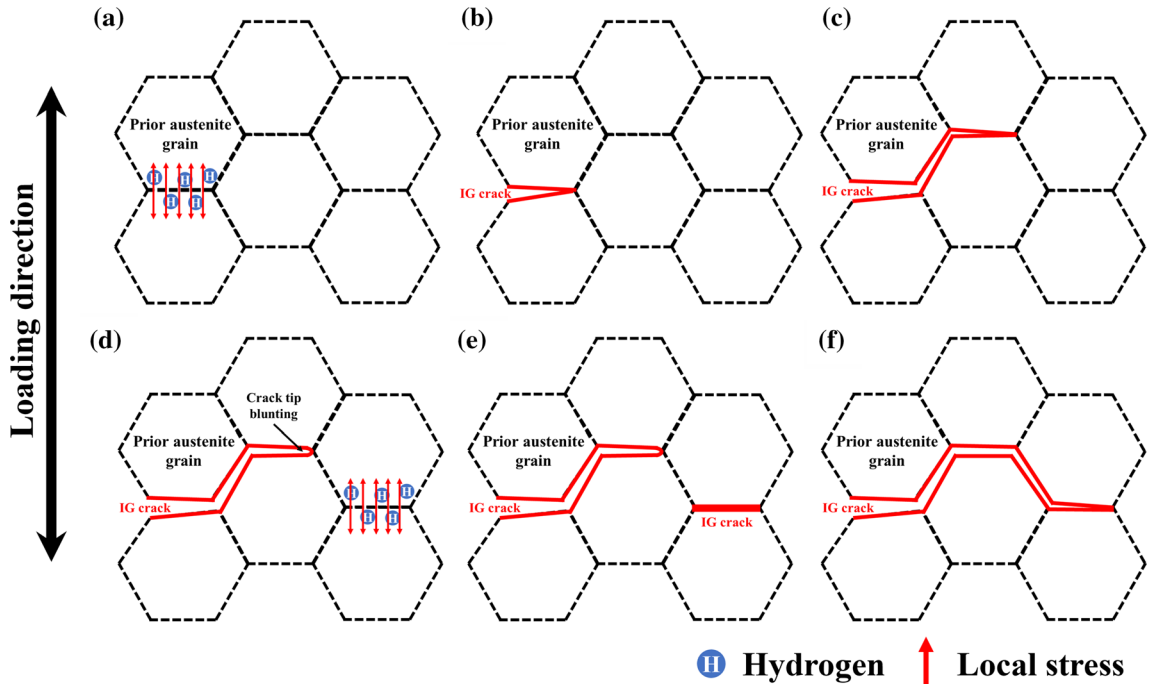

Fig. 15—Schematic illustration for the IG crack growth process. (*a*) Evolution of local stress and hydrogen accumulation. (*b*) Cracking and (*c*) crack growth along the prior austenite grain boundary. (*d*) Crack blunting and hydrogen accumulation at a prior austenite grain boundary where local stress effectively acts. (*e*) Sub-crack initiation in front of the main crack tip. (*f*) Crack growth through crack coalescence.

the IG cracks [Figure 7(d)] due to the larger macroscopic strain, which indicates that the IG-like crack growth occurred in the highly plastically deformed region compared to the IG crack growth. These results indicate that the plasticity effect on crack growth is the key to understanding IG-like fracture behavior.

Similar to the IG crack, the IG-like crack growth also showed a discontinuity process at the micron scale. In addition, the IG-like crack growth involved the formation of nano-voids and subsequent growth and coalescence with the main crack, as shown in Figure 12. This behavior is consistent with previous studies on hydrogen-related crack growth along grain boundaries. Specifically, hydrogen-assisted crack growth in general steels, such as ferritic steel,[46] ferrite/bainite steel,[47] austenitic steel,[48] and martensitic steel,[29,49] occurs via coalescence of the main crack and nano-cracks/voids. As mentioned in Section III–C, the nano-voids formed and grew on the side where the block alignment was significantly inclined to the grain boundary. In addition, the spacing of the nano-voids was approximately the same or lower than the transverse block size, according to the SE image and IPF map [Figures 12(c) and (d)]. Michiuchi *et al.*[50] reported that inter-lath slip systems, which glide on the slip plane parallel to the habit plane, are preferentially activated in lath martensitic steel under tensile loading. Mine 51 reported that the critical resolved shear stress of inter-lath slip systems is significantly lower than that of trans-lath slip systems across the habit plane. Therefore, activation of the slip systems parallel to the block alignment resulted in dislocation pile-up against the prior austenite grain boundary, which occurred particularly when the block alignment was inclined to the grain boundary, as schematically shown in Figure 16(a). The dislocation pile-up caused stress concentration at the grain boundary, with which dislocation-transported hydrogen and weakly trapped hydrogen induced a nano-void on one side of the grain boundary [Figure 16(b)]. Dislocation effects have been discussed as hydrogen-enhanced localized plasticity-mediated decohesion mechanisms.[29,52,53] Furthermore, the block boundary, as the effective grain boundary in lath martensite, not only suppressed the trans-lath slip activities, but also prevented crack growth, resulting in crack tip blunting. With local plastic deformation at the crack tip, the nano-voids ahead of the crack tip also grew, as shown in Figure 16(c). Because dislocation-pile-up-induced nano-void formation occurs in every block as long as the slip systems along the block are activated, the spacing of nano-voids becomes similar to or less than the transverse block size. It is noteworthy that the local plastic strain shown in the KAM map [Figure 12(e)] was high in the crack coalescence region. In addition, the IG-like cracks opened irregularly (Figure 13), which indicates that the Mode-I loading heterogeneously contributed to the crack tip deformation. In this context, it is plausible to assume that the local crack opening displacement is high when crack blunting occurs and is low when the crack propagates through coalescence with nano-voids. Therefore, these results indicate that the sub-micron-scale IG-like crack growth occurs via the repetition of crack blunting and coalescence of the crack tip and nano-voids by plasticity-induced tearing of the ligament. That is, when the nano-voids grew to a threshold size, the crack re-grew by tearing of the ligament between the blunt crack tip

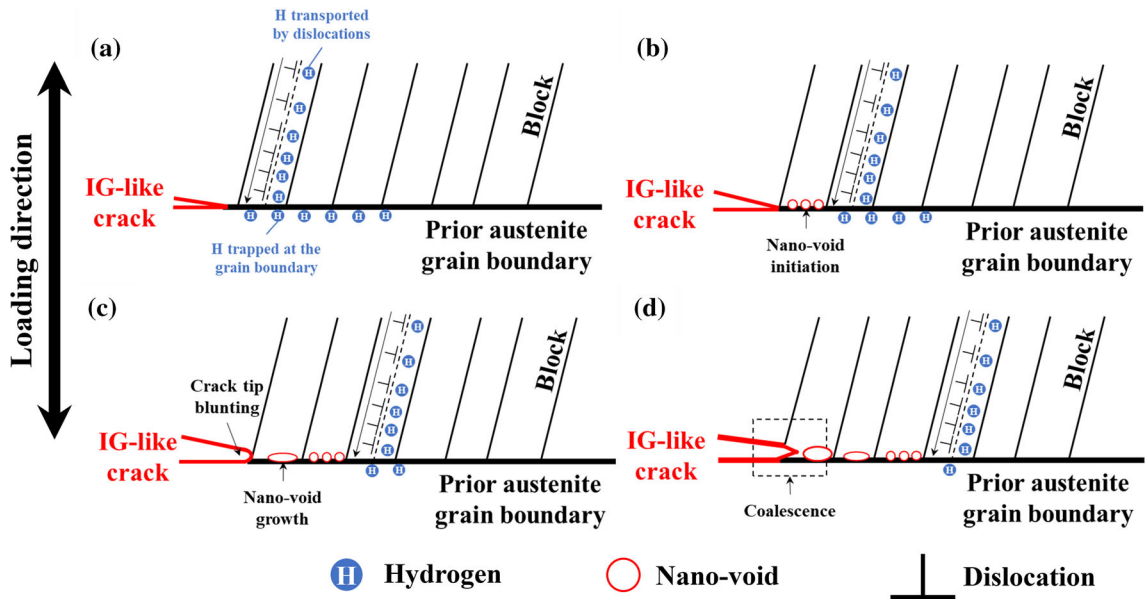

Fig. 16—Schematics for the IG-like crack growth process. (*a*) Dislocation motion and hydrogen accumulation near the crack tip. (*b*) Nano-void initiation. (*c*) Crack tip blunting and nano-void growth. (*d*) Crack-nano-void coalescence and further dislocation-driven nano-void formation.

and the enlarged nano-void under an elevated tensile loading [Figure 16(d)]. Because the tearing of the ligament is not a brittle phenomenon, nano-void coalescence occurred within the grain along the prior austenite grain boundary, as observed in Figures 12(c) and (d), which is similar to previous reports.[49,54] Because the nano-void formation and subsequent coalescence arose from the plasticity evolution at the crack tip, the size of these nano-voids decreased with the distance from the crack tip, as shown in Figures 12(b) and (c).

The morphological features of the IG-like crack also support the significance of the plasticity effect on the crack growth. The IPF map [Figure 13(b)] exhibited a tortuous crack shape in either the IG-like fracture region or the TG fracture region, similar to the ductile fracture.[55] This tortuous shape of the IG-like crack and relatively high KAM values beneath the cracked prior austenite grain boundaries in Figures 13(a) and (c) indicate the IG-like crack growth accompanying the obvious plastic deformation of the grain boundary. Based on the comparison between IG fracture and IG-like fracture, the difference in the two fracture modes is attributed to the difference in the degree of contribution of plasticity to the IG crack formation/growth.

C. *Origins of the Rough Crack Surface and Tear Ridges in the IG-Like Fracture*

The IG-like fracture surface shown in Figure 5(d) was rough and exhibited tear ridges. In fact, the tear ridge is one of the typical morphological features of hydrogen-assisted QC fracture in lath martensite, which is highly relevant to the interaction between the crack and hierarchical microstructure characteristics (*i.e.,* crack branching/deflection along the lath/block boundaries).[21] Therefore, the influence of the hierarchical microstructure on the IG-like crack growth is key to understanding the formation mechanism of the tear ridges on IG-like fracture surfaces. When decohesion controls cracking, remote stress, elastic strain incompatibility, cohesive energy, and crack tip stress field are detrimental factors. Compared with the factors controlling decohesion, the plasticity evolution is highly microstructure-dependent and thus heterogeneous particularly in the lath martensitic microstructure. Therefore, as long as plasticity plays a significant role in crack growth, the cracking behavior becomes microstructure-sensitive and discontinuous, which acts as a factor that stops the growth or causes crack branching/deflection. In the present case, the presence of a prior austenite grain boundary and the block size/alignment were the crucial factors; accordingly, crack branching/deflection at grain boundary triple junctions at the micron scale and along block alignments at the sub-micron scale were observed when IG-like fracture occurred, as shown in Figure 14. Because the spacing of these crack branches at the sub-micron scale was similar to the spacing of the tear ridges on the IG-like fracture surface (0.5 to 1.0 μm), the crack branching along the block boundaries could also be one of the causes of the tear ridge formation.

V. CONCLUSIONS

In this study, hydrogen-assisted IG and IG-like fractures in tempered lath martensitic steel were comparatively characterized in terms of microstructural plasticity and crack morphology. The major conclusions are as follows.

(1) The IG fracture occurred in the elastic regime, and a significant portion of the fracture surface showed smooth regions. The crack growth was

discontinuous at the micron scale (grain size scale), and the preferential microstructure that stopped the crack growth was triple junctions of the prior austenite grain boundary. In front of the non-propagating crack tip, a sub-crack initiated, and subsequent coalescence between the non-propagating crack tip and sub-crack enabled further crack growth.

(2) When the introduced hydrogen content was reduced, an IG-like fracture occurred. Plasticity significantly evolved macroscopically and microscopically under hydrogen-charging conditions. In IG-like fracture, discontinuous crack growth occurs at the micron scale and sub-micron scale (scale of transverse block size). The interaction between dislocation slip along the block boundaries and prior austenite grain boundary plausibly caused nano-voids in the vicinity of the crack tip. Coalescence of the main crack and nano-voids resulted in IG-like crack growth along prior austenite grain boundaries at the sub-micron scale. The nano-void formation and subsequent coalescence with nano-voids caused tear ridges on the IG-like fracture surface.

(3) Plasticity effects in the IG-like crack growth caused a rough crack surface at the sub-micron scale. One of the cases involved the coalescence of the nano-voids by tearing the ligament. Therefore, the coalescence of the nano-voids occurred within the prior austenite grain but near the grain boundary. The other factor was crack branching/deflection along the block boundaries, which was due to the prevention of dislocation slip and crack growth at the boundaries.

ACKNOWLEDGMENTS

This work was supported financially by JSPS KAKENHI (JP20H02457) and a research project entitled "Mechanism from incubation period to fracture in hydrogen embrittlement of high-strength steels" and funded by the Iron and Steel Institute of Japan (ISIJ).

CONFLICT OF INTEREST

Other than those financial supports mentioned above, on behalf of all authors, the corresponding author states that there is no conflict of interest.

REFERENCES

1. G. Krauss and A.R. Marder: *Metall. Trans.*, 1971, vol. 2, pp. 2343–57.
2. S. Morito, H. Tanaka, R. Konishi, T. Furuhara, and T. Maki: *Acta Mater.*, 2003, vol. 51, pp. 1789–99.
3. H. Kitahara, R. Ueji, N. Tsuji, and Y. Minamino: *Acta Mater.*, 2006, vol. 54, pp. 1279–88.
4. J.W. Morris, C. Kinney, K. Pytlewski, and Y. Adachi: *Sci. Technol. Adv. Mater.*, DOI: https://doi.org/10.1088/1468-6996/14/1/014208.
5. T. Ohmura, A.M. Minor, E.A. Stach, and J.W. Morris: *J. Mater. Res.*, 2004, vol. 19, pp. 3626–32.
6. M. Nagumo: *Fundamentals of Hydrogen Embrittlement*, 1st ed. Springer, Tokyo, 2016.
7. M.L. Martin, J.A. Fenske, G.S. Liu, P. Sofronis, and I.M. Robertson: *Acta Mater.*, 2011, vol. 59, pp. 1601–06.
8. C.J. McMahon Jr.: *Eng. Fract. Mech.*, 2001, vol. 68, pp. 773–88.
9. Y. Matsumoto and K. Takai: *Metall. Mater. Trans. A.*, 2018, vol. 49A, pp. 490–97.
10. Y. Matsumoto, K. Takai, M. Ichiba, T. Suzuki, T. Okamura, and S. Mizoguchi: *ISIJ Int.*, 2013, vol. 53, pp. 714–22.
11. Y. Matsumoto and K. Takai: *Metall. Mater. Trans. A.*, 2017, vol. 48A, pp. 666–77.
12. G. Ming and R.P. Wei: *Acta Metall.*, 1984, vol. 32, pp. 2115–24.
13. Y.H. Kim and J.W. Morris: *Metall. Trans. A.*, 1983, vol. 14A, pp. 1883–88.
14. P. Lejček: *Springer Ser. Mater. Sci.*, 2010, vol. 136, pp. 173–201.
15. G.C. Allen and R.K. Wild: *Philos. Mag. A.*, 1986, vol. 54, pp. L37-l42.
16. P. Novak, R. Yuan, B.P. Somerday, P. Sofronis, and R.O. Ritchie: *J. Mech. Phys. Solids.*, 2010, vol. 58, pp. 206–26.
17. L. Cho, P.E. Bradley, D.S. Lauria, M.L. Martin, M.J. Connolly, J.T. Benzing, E.J. Seo, K.O. Findley, J.G. Speer, and A.J. Slifka: *Acta Mater.*, 2021, vol. 206, p. 116635.
18. K. Saito, T. Hirade, and K. Takai: *Metall. Mater. Trans. A.*, 2019, vol. 50A, pp. 5091–102.
19. A. Nagao, C.D. Smith, M. Dadfarnia, P. Sofronis, and I.M. Robertson: *Procedia Mater. Sci.*, 2014, vol. 3, pp. 1700–05.
20. K. Ogawa, Y. Matsumoto, H. Suzuki, and K. Takai: *ISIJ Int.*, 2019, vol. 59, pp. 1705–14.
21. T. Chen, T. Chiba, M. Koyama, A. Shibata, E. Akiyama, and K. Takai: *Metall. Mater. Trans. A.*, 2021, vol. 52A, pp. 4703–13.
22. M. Yamaguchi, J. Kameda, K.I. Ebihara, M. Itakura, and H. Kaburaki: *Philos. Mag.*, 2012, vol. 92, pp. 1349–68.
23. J.R. Rice, Z. Suo, and J.-S. Wang: *Met. Interfaces.*, 1990, vol. 4, pp. 269–94.
24. M. Nagumo and H. Matsuda: *Philos. Mag. A.*, 2002, vol. 82, pp. 3415–25.
25. H.K. Birnbaum and P. Sofronis: *Mater. Sci. Eng. A.*, 1994, vol. 176, pp. 191–202.
26. T. Matsumoto, J. Easrman, and H.K. Birnbaum: *Scr. Mater.*, 1981, vol. 15, p. 5.
27. P. Sofronis, Y. Liang, and N. Aravas: *Eur. J. Mech. A.*, 2001, vol. 20, pp. 857–72.
28. I.M. Robertson: *Eng. Fract. Mech.*, 2001, vol. 68, pp. 671–92.
29. A. Nagao, M. Dadfarnia, B.P. Somerday, P. Sofronis, and R.O. Ritchie: *J. Mech. Phys. Solids.*, 2018, vol. 112, pp. 403–30.
30. A. Shibata, H. Takahashi, and N. Tsuji: *ISIJ Int.*, 2012, vol. 52, pp. 208–12.
31. M. Ohori, T. Chiba, Y. Matsumoto, H. Suzuki, and K. Takai: *IOP Conf. Ser. Mater. Sci. Eng.*, 2018, vol. 461, p. 012062.
32. K. Takai and R. Watanuki: *ISIJ Int.*, 2003, vol. 43, pp. 520–26.
33. M. Wang, E. Akiyama, and K. Tsuzaki: *Corros. Sci.*, 2007, vol. 49, pp. 4081–97.
34. D. Stojakovic: *Process. Appl. Ceram.*, 2012, vol. 6, pp. 1–13.
35. M. Nagumo and K. Takai: *Acta Mater.*, 2019, vol. 165, pp. 722–33.
36. M. Calcagnotto, D. Ponge, E. Demir, and D. Raabe: *Mater. Sci. Eng. A.*, 2010, vol. 527, pp. 2738–46.
37. S. Dejan: *Process. Appl. Ceram.*, 2012, vol. 6, pp. 1–13.
38. A. Shibata, T. Yonemura, Y. Momotani, M. Heom Park, S. Takagi, Y. Madi, J. Besson, and N. Tsuji: *Acta Mater.*, 2021, vol. 210, p. 116828.
39. Y. Takeda and C.J. McMahon: *Metall. Trans. A.*, 1981, vol. 12A, pp. 1255–66.
40. Y. Momotani, A. Shibata, D. Terada, and N. Tsuji: *Int. J. Hydrogen Energy.*, 2017, vol. 42, pp. 3371–79.
41. K. Takai, J. Seki, and Y. Homma: *Mater. Trans. JIM.*, 1995, vol. 36, pp. 1134–39.
42. A. Shibata, T. Murata, H. Takahashi, T. Matsuoka, and N. Tsuji: *Metall. Mater. Trans. A.*, 2015, vol. 46, pp. 5685–96.

43. S.F. Anis, M. Koyama, S. Hamada, and H. Noguchi: *Theor. Appl. Fract. Mech.*, 2020, vol. 107, p. 102561.
44. Y.Z. Wang, J.D. Atkinson, R. Akid, and R.N. Parkins: *Fatigue Fract. Eng. Mater. Struct.*, 1996, vol. 19, pp. 427–39.
45. V. Venegas, F. Caleyo, T. Baudin, J.M. Hallen, and R. Penelle: *Corros. Sci.*, 2009, vol. 51, pp. 1140–45.
46. K. Okada, A. Shibata, Y. Takeda, and N. Tsuji: *Int. J. Hydrogen Energy.*, 2018, vol. 43, pp. 11298–306.
47. T. Homma, S. Anata, S. Onuki, and K. Takai: *ISIJ Int.*, 2021, vol. 61, pp. 2654–65.
48. M. Koyama, K. Habib, T. Masumura, T. Tsuchiyama, and H. Noguchi: *Int. J. Hydrogen Energy.*, 2020, vol. 45, pp. 10209–18.
49. A. Shibata, Y. Momotani, T. Murata, T. Matsuoka, M. Tsuboi, and N. Tsuji: *Mater. Sci. Technol.*, 2017, vol. 33, pp. 1524–32.
50. M. Michiuchi, S. Nambu, Y. Ishimoto, J. Inoue, and T. Koseki: *Acta Mater.*, 2009, vol. 57, pp. 5283–91.
51. Y. Mine, K. Hirashita, H. Takashima, M. Matsuda, and K. Takashima: *Mater. Sci. Eng. A.*, 2013, vol. 560, pp. 535–44.
52. A. Nagao, C.D. Smith, M. Dadfarnia, P. Sofronis, and I.M. Robertson: *Acta Mater.*, 2012, vol. 60, pp. 5182–89.
53. M.B. Djukic, G.M. Bakic, V. Sijacki Zeravcic, A. Sedmak, and B. Rajicic: *Eng. Fract. Mech.*, 2019, p. 106528.
54. A. Shibata, Y. Madi, K. Okada, N. Tsuji, and J. Besson: *Int. J. Hydrogen Energy.*, 2019, vol. 44, pp. 29034–46.
55. T.L. Anderson: *Fracture Mechanics: Fundamentals and Applications*, CRC Press, New York, 2004.

Publisher's Note Springer Nature remains neutral with regard to jurisdictional claims in published maps and institutional affiliations.